AIAA 81-1492R

Comparison of Computational and Experimental Jet Effects

J. L. Jacocks,* W. L. Peters,† and F. C. Guyton‡
Calspan Field Services, Inc., Arnold Air Force Station, Tennessee

Computations were made for transonic flow over a nozzle afterbody with a real plume. The effects of parameters such as nozzle pressure ratio, plume stagnation temperature, and interior nozzle shape on afterbody drag were quantified and compared with available experimental data. Remarkable agreement between the computational and experimental results is demonstrated, including the drag minimum associated with low nozzle pressure ratios and the absolute dependence of drag on temperature. The computer program used for the calculations is an axisymmetric modification of Deiwert's planar Navier-Stokes program and utilizes a mixed explicit-implicit MacCormack algorithm with an algebraic turbulence model.

Nomenclature

A = nozzle area, in.^{2}
A_e/A^* = nozzle exit-to-throat area ratio
C_D = afterbody pressure drag coefficient
C_p = afterbody pressure coefficient
D_I/D_e = maximum inviscid jet plume boundary diameter divided by nozzle exit diameter, where D_I is obtained from the isentropic area ratio function for a flow expanded to freestream static pressure; i.e., $D_I = f(p_\infty, P_{t_j}, \gamma_j)$
M = Mach number
NPR = nozzle total-to-freestream static pressure ratio $= P_{t_j}/P_\infty$
P = static pressure, psia
P_t = total pressure, psia
q = dynamic pressure, psi
Re = freestream Reynolds number per foot
S_b = maximum model cross-sectional area
T_t = total temperature, °R
γ = ratio of specific heats
θ_N = nozzle divergence half-angle, deg

Subscripts and Superscript

I = jet conditions at inviscid jet plume boundary
e = jet conditions at nozzle exit plane
j = jet conditions at any given axial location
∞ = freestream conditions
$*$ = jet conditions at nozzle throat

Introduction

CURRENTLY, estimates of nozzle-afterbody drag for the design of the new aircraft are generated primarily in wind tunnel tests, rather than by analysis, because accurate computational methods treating transonic freestream conditions and incorporating real plume effects have been slow to develop. Wind tunnel experiments are used to measure effects caused by nozzle pressure ratio, nozzle geometry, and freestream Mach number variations. But wind tunnel results occasionally require corrections to account for support system interference and cold flow jet simulation errors. In addition, the large test matrices required to analyze the many effects which influence the nozzle-afterbody performance of aircraft are expensive to obtain.

With reliable computational results, wind tunnel test matrices can be reduced to a few select data points. In addition, flowfield analysis of both the freestream and the jet is made possible, allowing examination of effects, such as jet temperature, which are difficult to obtain in the wind tunnel. A computer code for performing such analyses has been developed using a numerical solution of the Navier-Stokes equations for axisymmetric flow over nozzle afterbodies with either real or simulated plumes.[1]

The purpose of the present study is to demonstrate the capabilities and limitations of this code in the prediction of nozzle-afterbody pressure distributions and drag as compared to experimental data with a variation of jet and freestream properties and nozzle geometry.

Description of Wind Tunnel Experiments

The experimental data used for comparison with computational results were acquired in the Arnold Engineering Development Center 16-ft Transonic Wind Tunnel (16T) with a strut-supported axisymmetric model configuration. A sketch showing basic model and support strut details in the 16T tunnel is presented in Fig. 1. Testing was conducted at freestream Mach numbers from 0.6 to 1.5, and the freestream Reynolds number was varied from 1.0 to 5.0 million per foot.

The external afterbody contour of the model configurations tested and used in computations was the AGARD 15-deg boattail. Unlike the computational model, the experimental configurations, shown in Fig. 2, had a finite nozzle base thickness to allow incorporation of surface pressure orifices at the end of the boattail. A more complete description of the wind tunnel experiments conducted with each test model configuration may be found in the associated reference material listed in Fig. 2.

The test model boattail was instrumented with surface static pressure orifices, and the afterbody pressure drag coefficient was determined by numerically integrating pressures located along the top centerline of the model in an effort to minimize the effect of strut interference. For all experiments (as well as for computations), the drag coefficient was based on the maximum model cross-sectional area, and the integrated area excluded nozzle base area. An estimate of the experimental data repeatability, that is a measure of data reliability for afterbody drag coefficient is ± 0.0017 and for pressure coefficient it is ± 0.0020.

Presented as Paper 81-1492 at the AIAA/SAE/ASME 17th Joint Propulsion Conference, Colorado Springs, Colo., July 27-29, 1981; submitted Aug. 24, 1981; revision received Feb. 12, 1982.

*Supervisor, Computational Fluid Dynamic Section, Projects Branch, AEDC Division, Propulsion Wind Tunnel. Member AIAA.

†Project Engineer, Projects Branch, AEDC Division, Propulsion Wind Tunnel.

‡Project Engineer, Projects Branch, AEDC Division, Propulsion Wind Tunnel. Member AIAA.

Description of Computational Techniques

The axisymmetric mass-averaged Navier-Stokes equations, coupled with the perfect gas equation of state and a suitable turbulence model have been solved[1] using finite volume flux-balancing techniques. The code is based on the two-dimensional airfoil program of Deiwert,[6] and the solution algorithm is an unsplit version of MacCormack's[7] predictor-corrector scheme. The two-layer algebraic turbulence model of Baldwin and Lomax[8] is used for both the plume mixing region and solid surfaces. The following paragraphs briefly describe the computational mesh, solution algorithm, and boundary conditions.

A representative computational mesh is given in Fig. 3. This is an exploded picture of the afterbody. The computational boundaries extend beyond this view. A fine exponentially stretched mesh is construed to be parallel to the body surface and extends into the wake/plume region with the first node point within the viscous sublayer. Coarser mesh point spacing is specified in regions of reduced viscous effects, with radial exponential stretching in the outer flow and proportionate radial spacing within the plume. Note that the afterbody nozzle is, in effect, treated as an airfoil trailing edge with a conventional C-type mesh. The outer boundary is approximately nine body radii from the body surface. The mesh normal to the centerline is parallel. There is close spacing over the afterbody for accuracy in drag integration, with the heaviest concentration around the trailing edge where the significant changes in the flow are realized. In the plume region, the vertical mesh becomes coarser moving downstream where less accuracy is required. The boundaries in the flow direction are approximately six and five body radii upstream and downstream from the trailing edge, respectively, for a total of approximately 3300 grid points. Although the influences of boundary proximity on the computational results have not been thoroughly defined, it is believed to be minimal.

The flowfield is advanced in time using two coupled methods. In regions of relatively coarse mesh spacing the explicit MacCormack predictor-corrector method without flux splitting is applied. In the fine mesh regions the radial flux balance is obtained by solving the inviscid hyperbolic part of the equations using the method of characteristics and the viscous part with an implicit scheme which was also developed by MacCormack.[9] Longitudinal fluxes in the fine mesh are computed explicitly.

Boundary conditions are incorporated using dummy mesh points exterior to the computational region. Freestream conditions are specified at the outer boundary with zero-gradient outflow conditions downstream. Solid surfaces use zero-slip, adiabatic-wall conditions with zero normal derivative on pressure. Communication between the two fine-mesh regions within the plume is obtained with overlap continuity. Centerline boundary conditions are a reflection with the axisymmetric singularity avoided by simply requiring the mesh boundary to be coincident with the centerline. The outer stream inflow boundary condition is freestream with specified boundary-layer integral properties and the turbulent velocity profile of Whitfield.[10] The inner inflow boundary condition uses characteristic relations with specified stagnation pressure and temperature and negligible viscous effects.

Most of the computational results presented were obtained using the CRAY-1 of United Computing Services. Computer time ranged from 30 min for a supersonic condition at design nozzle pressure ratio to 1 h or more for some subsonic freestream conditions with off-design nozzle flow. Convergence of the solution to steady state was determined by monitoring the afterbody drag. Incremental solutions were usually obtained by restarting a known solution with perturbations in jet stagnation conditions.

Analysis and Results

A variety of effects on afterbody pressure distributions and drag are compared with predictions from the code and ex-

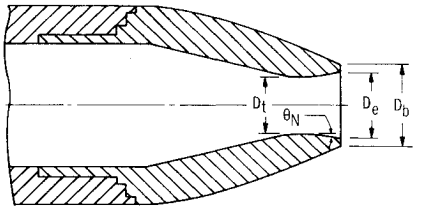

Ref.	Config.	D_b, in.	D_e, in.	D_t, in.	θ_N, deg	A_e/A^*	Tunnel
2	1*	4.092	3.918	3.550	2.5	1.219	16T
2	2*	4.092	3.902	3.530	5.1	1.222	16T
2	3*	4.092	3.888	3.530	10.0	1.213	16T
2	4	4.092	3.912	3.912	-0-	1.000	16T
2	5*	4.092	3.940	3.244	5.0	1.475	16T
2	6	4.092	3.230	3.230	-6.1	1.000	16T
3	7	4.092	3.822	3.822	-0-	1.000	16T
3	8	4.092	3.820	3.587	5	1.135	16T
3	9	4.092	3.822	3.459	5	1.221	16T
3	10	4.092	3.824	3.354	5	1.300	16T
3	11	4.092	3.823	3.132	5	1.487	16T
5	12	4.092	3.900	3.900	-7	1.000	16T
-	13*	3.958	3.715	3.667	0.484	1.026	16T

*Experimental configurations for which computational models were developed.

(Note: For computations $D_e - D_b$ and A_e/A^* and θ_N held constant).

Fig. 2 Nozzle geometries.

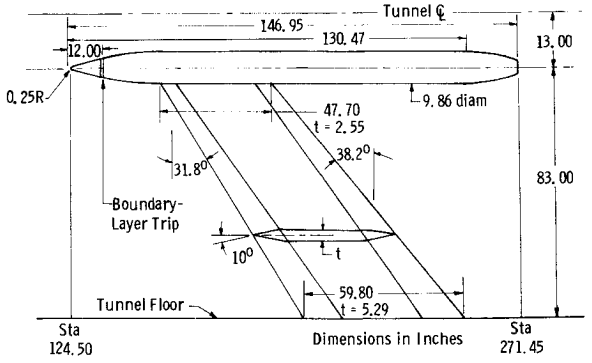

Fig. 1 Basic model dimensions.

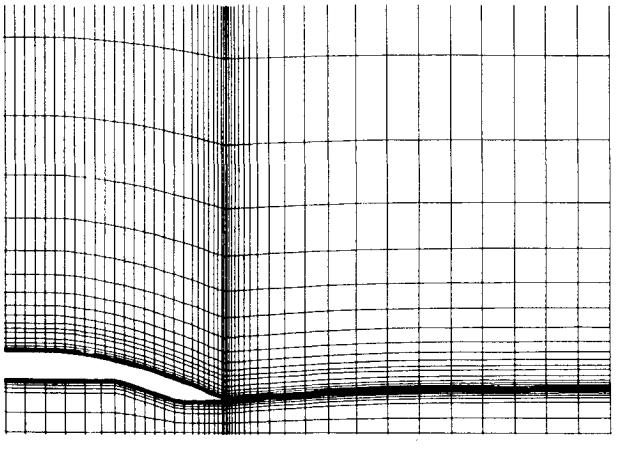

Fig. 3 Representative computational mesh.

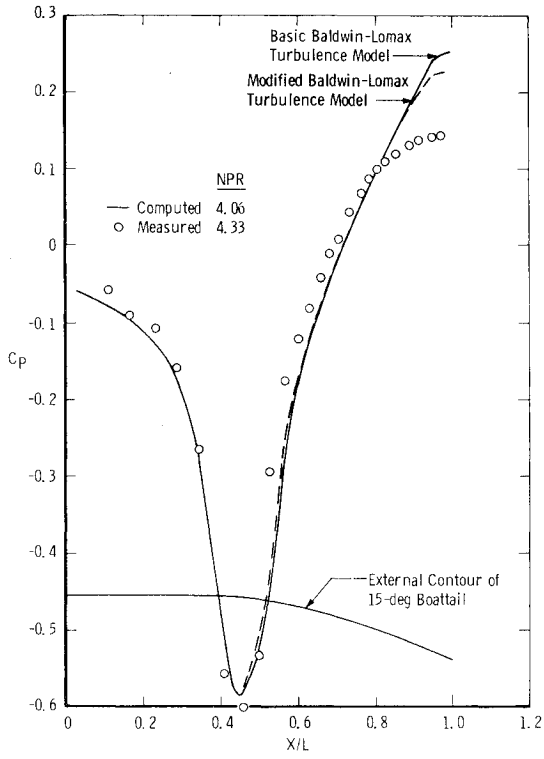

Fig. 4 Comparison of computational and experimental afterbody pressure distributions, CONF2, $M_\infty = 0.9$, $Re = 1.5 \times 10^6$.

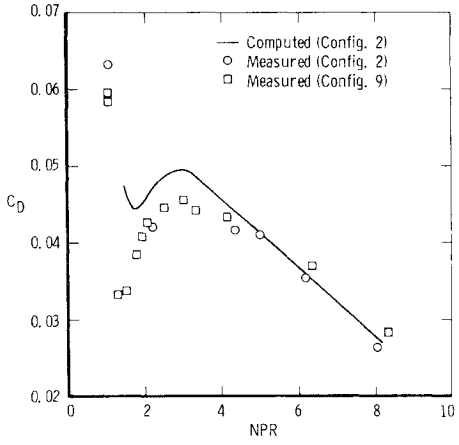

Fig. 5 Effect of nozzle pressure ratio on afterbody drag coefficient, $M_\infty = 0.9$, $Re = 1.5 \times 10^6$.

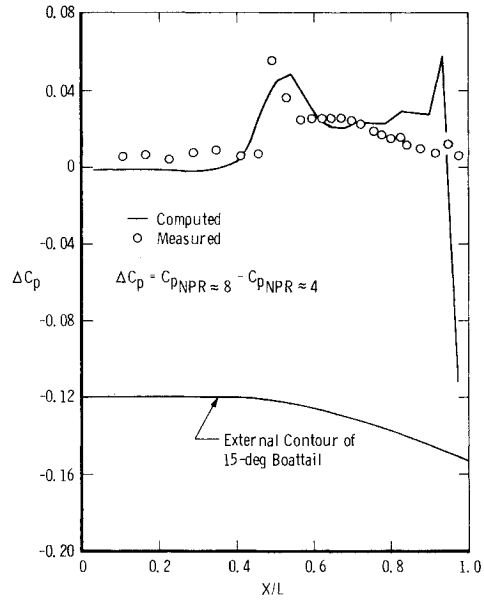

Fig. 6 Effect of nozzle pressure ratio on afterbody pressures, $M_\infty = 0.9$, $Re = 1.5 \times 10^6$.

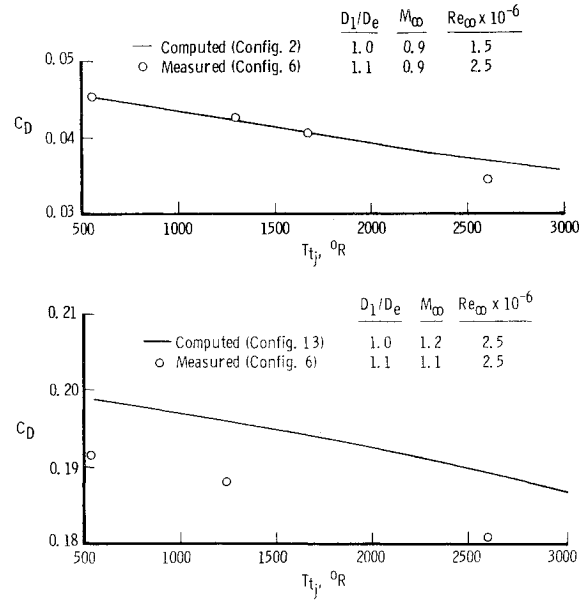

Fig. 7 Effect of jet total temperature on afterbody drag coefficient.

perimental data. The independent variable effects presented include nozzle pressure ratio, jet temperature, nozzle geometry, Reynolds number, and Mach number. Nozzle geometry effects include nozzle divergence angle and nozzle area ratio.

In general, absolute value comparisons of computational and experimental pressure distributions and drag coefficient data presented herein are not valid. The experimental data include the effects of nozzle base thickness and model strut-support interference that are not treated by the computational model. Conversely, computational models were not developed to correspond to the variety of internal nozzle geometries represented by the experimental configurations listed in Fig. 2. Therefore comparisons of experimental and computational data herein will, in general, be limited to analyzing incremental effects.

Jet Property Effects

One configuration, CONF2, was chosen as a baseline configuration to generate a computational model for the jet property effects of jet pressure and jet temperature. This configuration had the smallest experimental base thickness, and strut interference effects were minimized, as discussed earlier, by determining drag coefficient from pressure distributions located on the top side of the model.

An absolute comparison of predicted and measured afterbody pressure distributions is presented for this configuration at a freestream Mach number 0.9 in Fig. 4. The jet conditions are approximately the same for predicted and measured results and represent an ambient temperature jet at design nozzle pressure ratio.

As illustrated in Fig. 4, the computed and measured surface pressure coefficients for the flow expansion region agree. In the recompression region, the predicted results indicate a higher pressure at the end of the afterbody than was measured. This difference may be attributed to the more direct effect of jet pressure at the end of the afterbody on the computational model since no base is present in the computations. The effect on the pressure distribution of modifying the turbulence model using vorticity-gradient

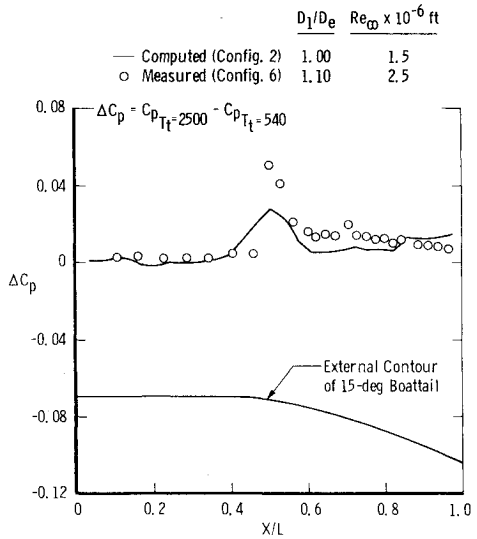

Fig. 8 Effect of jet total temperature on afterbody pressures, $M_\infty = 0.9$, D_1/D_e = const.

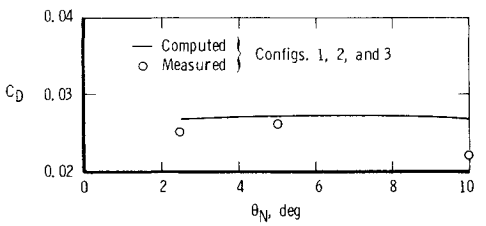

Fig. 9 Effect of nozzle divergence angle on afterbody drag coefficient, $M_\infty = 0.9$, NPR = 8.

relaxation[1] is also given in Fig. 4. Further improvement in the computed results could be obtained by tuning the turbulence model. However, to permit consistent results, all subsequent computations presented were obtained with the basic Baldwin-Lomax model.

Jet pressure effects, commonly represented as nozzle pressure ratio effects, are shown in Figs. 5 and 6 for configurations CONF2 and CONF9. In Fig. 5, the shape and absolute magnitude of the predicted and measured C_D vs NPR curve are similar. The computations correctly predict[3,4] that with increasing pressure ratio from the jet-off condition, an initial decrease in drag occurs to a low pressure ratio "drag bucket," followed by an increase in drag to a maximum jet-on "peak drag" point; then, a continuing decrease in drag is produced by the increasing underexpanded jet plume blockage. Absolute values of drag coefficient are in agreement in the underexpanded jet regime (NPR $\geq$ 4); however, computational results predict a higher drag coefficient at overexpanded jet conditions (by approximately 0.0050 at NPR = 2.28). This disagreement may be a result of a larger influence of jet entrainment for the computational model since no nozzle base region exists to mask the effects of the jet.

To emphasize jet effects, as opposed to computational/experimental comparisons, the incremental effect of NPR variation on the afterbody pressures is given in Fig. 6 (with reference to Fig. 4). Increasing nozzle pressure ratio from design NPR increases the static pressure over the entire boattail, thereby decreasing afterbody drag as both experimental and computational results display. Both types of data illustrate that jet effects are confined to the recompression (adverse pressure gradient) region with minimal effect on the expansion region.

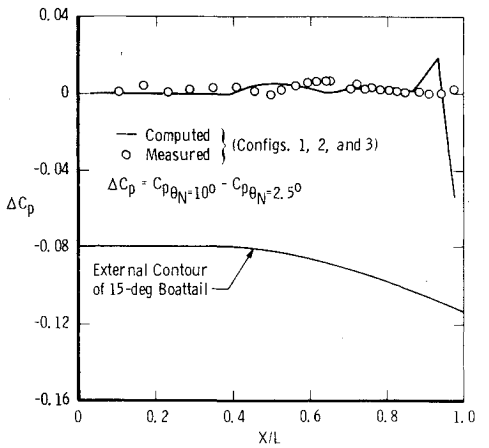

Fig. 10 Effect of nozzle divergence angle on afterbody pressures, $M_\infty = 0.9$, NPR = 0.9.

The effects of jet total temperature, T_{t_j}, are presented in Figs. 7 and 8. Large differences in nozzle base thickness and nozzle area ratio, as well as differences in nozzle flow parameters, make comparison of absolute drag coefficient and pressure coefficient levels meaningless. A further caution with respect to the comparisons relates to model surface temperatures. Computations were made at adiabatic wall conditions (hot interior and ambient exterior), whereas the experiments at elevated temperatures utilized nozzle cooling. Arbitrary wall temperatures can be specified in the code, but that option has not been exercised for this study. In Fig. 7, predicted and measured drag coefficient data are presented with the jet plume shape parameter, D_1/D_e, held fixed. The experimental data represent variations in T_{t_j}, including changes in γ_j for CONF6. The computational data are presented for CONF2 with T_{t_j} as a variable but with γ_j fixed. The effects of γ_j at fixed plume shape conditions (D_1/D_e) produce a negligible effect on nozzle-afterbody drag coefficient as shown in Ref. 4. Note that an experimental increase in T_{t_j} results in a linear decrease in drag coefficient that is predicted accurately by the code. Experimental and computational incremental pressure distributions in Fig. 8 support the results of Fig. 7. Again, jet effects are that an increase in T_{t_j} increases static pressure on the entire boattail, producing a larger recompression and decreased drag. Thus it is concluded that the code can be used to predict the afterbody drag coefficient sensitivity to jet temperature for axisymmetric aircraft nozzles.

Nozzle Geometry Effects

The effect of nozzle divergence angle at underexpanded jet conditions is shown in Figs. 9 and 10. Experimental and computational results are for configurations CONF1, CONF2, and CONF3 at a freestream Mach number of 0.9 and a nozzle pressure ratio of nominally 8. Similar to CONF2, the experimental nozzle base thickness was small for CONF1 and CONF3; therefore absolute values of predicted and measured drag coefficients are comparable.

In Fig. 9, experimental and computational values of drag coefficient are in agreement within 0.0050 and both indicate a small if not negligible effect of divergence angle. Pressure coefficient increments shown in Fig. 10 also illustrate no significant effect on divergence angle. This lack of influence indicates that jet simulation parameters that are functionally related to the divergence angle are not required for moderately expanded jets with nozzle configurations typical of aircraft at transonic speeds. Peters[2] made the same conclusion based on experimental evidence alone.

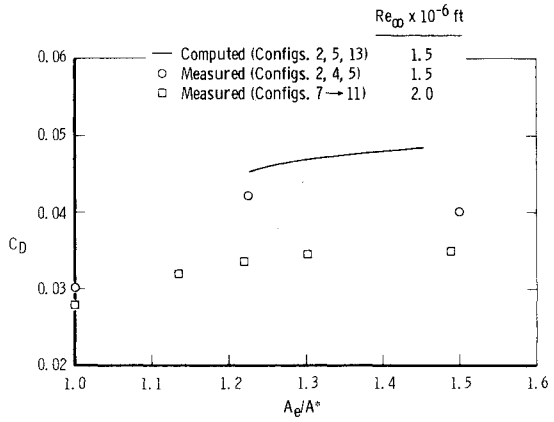

Fig. 11 Effect of nozzle area ratio on afterbody drag coefficient, $M_\infty = 0.9$, design NPR.

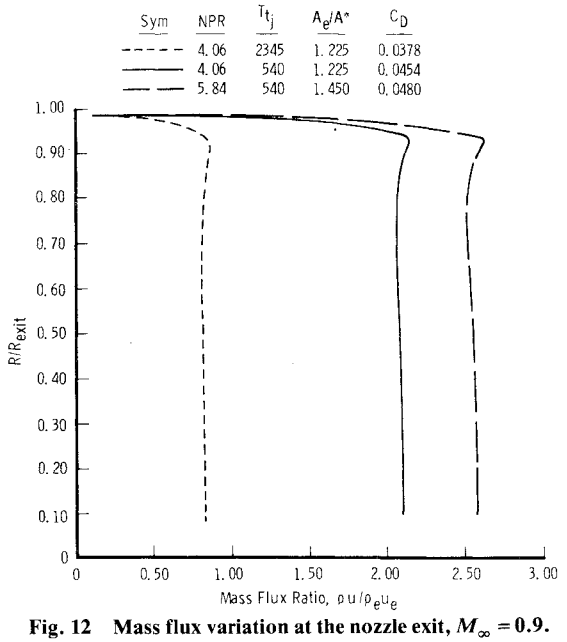

Fig. 12 Mass flux variation at the nozzle exit, $M_\infty = 0.9$.

The effect of the nozzle area ratio at design NPR ($D_j/D_e = 1$) is given in Fig. 11. Both the computational and experimental results indicate that increasing area ratio increases the afterbody drag coefficient. Again, although not shown, the effect of area ratio variation is primarily confined to the boattail region.

Computational Insights

Computer-generated flows offer significant additional information relative to wind tunnel experiments at "no additional cost." Detailed flowfield measurements are difficult to obtain in the wind tunnel, whereas computational results provide a medium whereby any desired data are easily obtained: the code user simply queries the solution(s) for the desired phenomena.

For example, detailed analysis[11] of experimental results has concluded that nozzle mass flux is a primary similarity parameter for afterbody drag. Supporting evidence is provided by the computations, with Fig. 12 giving the mass flux distribution across the nozzle plane for variations in jet temperature and nozzle area ratio. Increasing mass flux increases afterbody drag through entrainment as shown by the velocity profiles in Fig. 13.

However, it is also known that if the mass flux is increased by increasing the nozzle pressure ratio beyond design NPR, then plume blockage effects become dominant and cause a decrease in afterbody drag. Computed effects of increasing nozzle pressure ratio are shown by velocity profiles near the

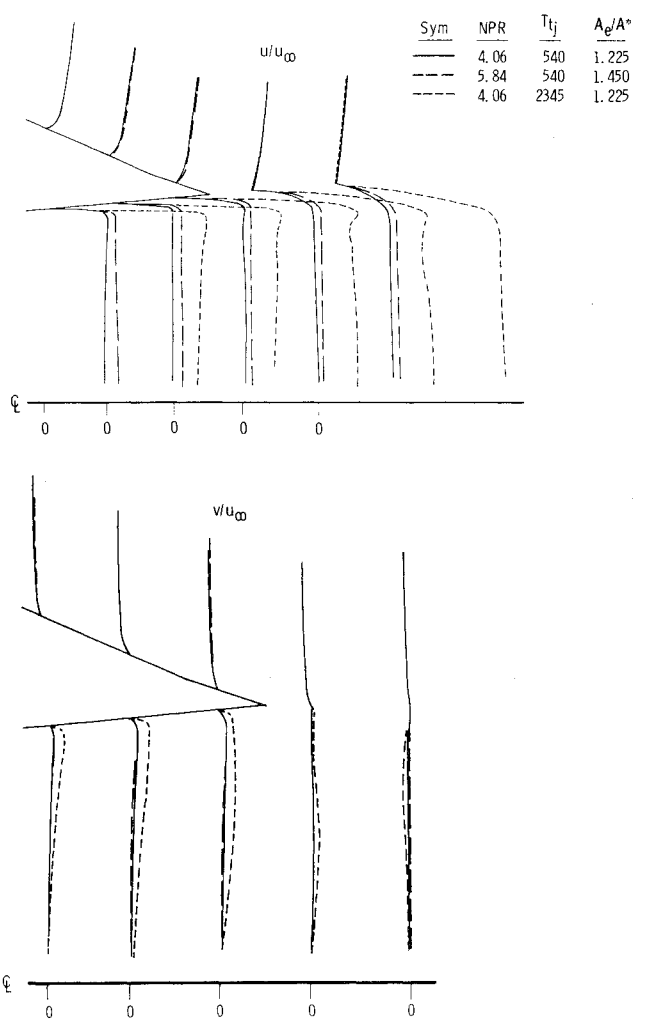

Fig. 13 Velocity profiles at the nozzle exit, $M_\infty = 0.9$.

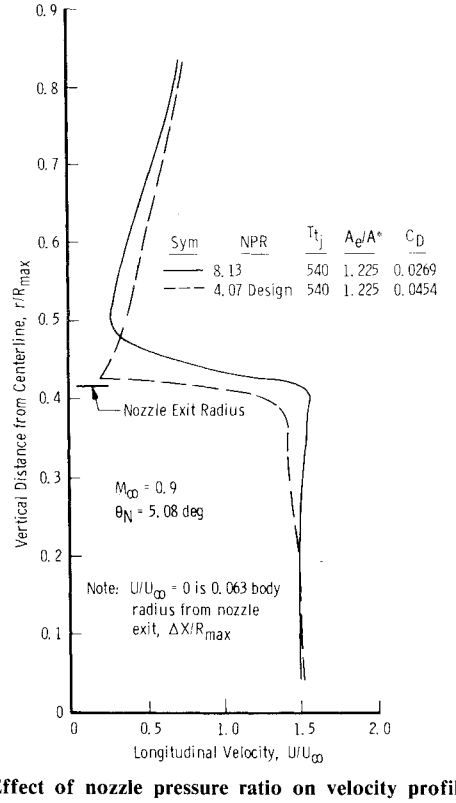

Fig. 14 Effect of nozzle pressure ratio on velocity profile at the nozzle exit, $M_\infty = 0.9$.

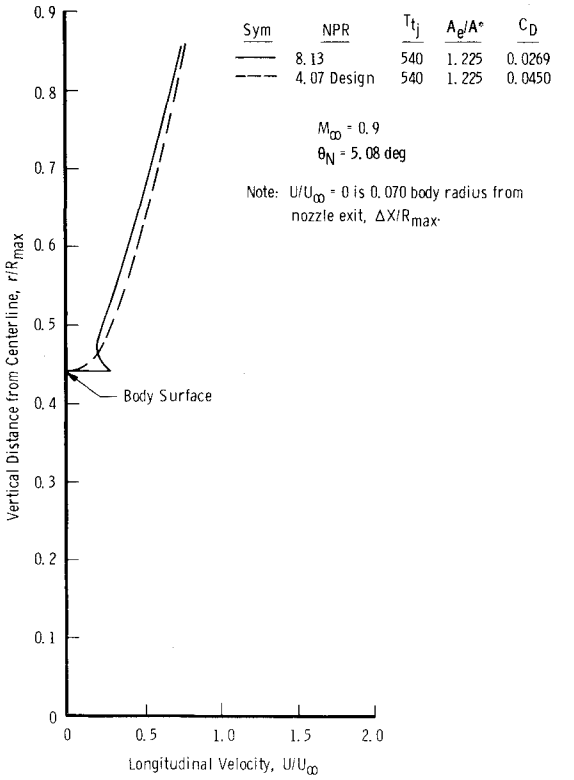

Fig. 15 Effect of nozzle pressure ratio on velocity profile at end of afterbody, $M_\infty = 0.9$.

nozzle exit in Figs. 14 and 15. Increased entrainment close to the plume and boattail is evident, but the outer flow is decelerated by downstream plume blockage effects which dominate the flowfield, resulting in increased static pressure and decreased drag.

Conclusions

A comparison of experimental afterbody pressure and drag coefficient data with computational results from an axisymmetric, Navier-Stokes code yields the following conclusions:

1) At transonic freestream Mach numbers, such as Mach number 0.9, the code correctly predicts the afterbody pressure coefficient distribution except at the trailing edge of the boattail. Differences in the experimental and computational nozzle base geometry may account for this disagreement.

2) At a freestream Mach number of 0.9, the code correctly predicts absolute values of afterbody drag coefficient (within 0.0050) over the full nozzle pressure ratio range.

3) The code correctly predicts the experimental incremental effects of jet temperature, nozzle divergence angle, and nozzle area ratio on afterbody drag coefficient.

References

[1] Jacocks, J.L., "Computation of Axisymmetric Separated Nozzle Afterbody Flow," AEDC-TR-79-71 (AD-A079694), Jan. 1980.

[2] Peters, W.L., "An Evaluation of Jet Simulation Parameters for Nozzle Afterbody Testing at Transonic Mach Numbers," AEDC-TR-76-109 (AD-A031525), Oct. 1976.

[3] Price, Earl A., "A Parametric Investigation of the Annular Jet Concept for Obtaining Afterbody Drag Data at Transonic Mach Numbers," AEDC-TR-77-104 (AD-A050891), Feb. 1978.

[4] Peters, W.L., "Jet Simulation Techniques: Simulation of Temperature Effects by Altering Gas Composition," AEDC-TR-78-43 (AD-A067084), March 1979.

[5] Galigher, L.L., Yaros, S.F., and Bauer, R.C., "Evaluation of Boattail Geometry and Exhaust Plume Temperature Effects on Nozzle Afterbody Drag at Transonic Mach Numbers," AEDC-TR-76-102 (AD-A030852), Oct. 1976.

[6] Deiwert, G.S., "Numerical Simulation of High Reynolds Number Transonic Flows" AIAA Paper 74-603, June 1974.

[7] MacCormack, R.W., "The Effect of Viscosity in Hypervelocity Impact Cratering," AIAA Paper 69-354, May 1969.

[8] Baldwin, B.S. and Lomax, H., "Thin Layer Approximation and Algebraic Model for Separated Turbulent Flows," AIAA Paper 78-257, Jan. 1978.

[9] MacCormack, R.W., "An Efficient Numerical Method for Solving the Time-Dependent Compressible Navier-Stokes Equations at High Reynolds Number," NASA TMX-73-129, July 1976.

[10] Whitfield, D.L., "Analytical Description of the Complete Two-Dimensional Turbulent Boundary-Layer Velocity Profile," AIAA Paper 78-1158, July 1978.

[11] Peters, W.L., "A Comparison of Jet Temperature Effects on Afterbody Drag with Those from Jet Molecular Weight and Nozzle Area Ratio Variations," AIAA Paper 80-1161, June 1980.